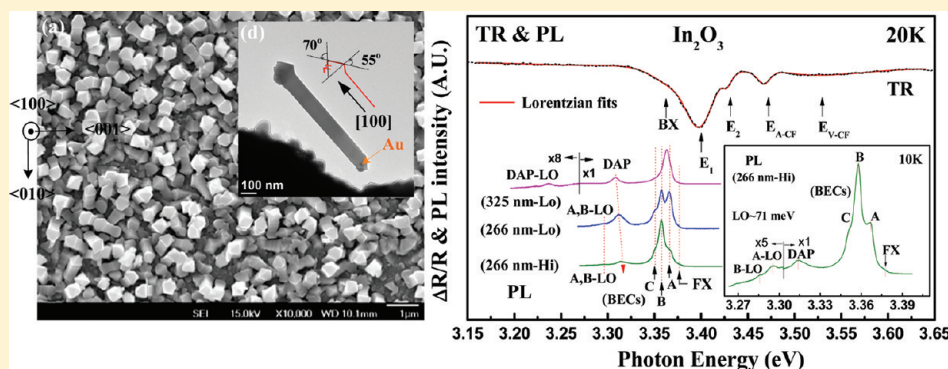


Direct Optical Observation of Band-Edge Excitons, Band Gap, and Fermi Level in Degenerate Semiconducting Oxide Nanowires  $\text{In}_2\text{O}_3$ Ching-Hwa Ho,<sup>\*,†,‡</sup> Ching-Hsiang Chan,<sup>‡</sup> Li-Chia Tien,<sup>§</sup> and Ying-Sheng Huang<sup>‡</sup><sup>†</sup>Graduate Institute of Applied Science and Technology and <sup>‡</sup>Department of Electronic Engineering, National Taiwan University of Science and Technology, Taipei 106, Taiwan<sup>§</sup>Department of Materials Science and Engineering, National Dong Hwa University, Shoufeng, Hualien 974, Taiwan

## ABSTRACT:



Direct optical evidence of Burstein–Moss shift (BMS) in conduction band of cubic  $c\text{-In}_2\text{O}_3$  nanowires is reported herein. The optical property of degenerate semiconducting oxide  $c\text{-In}_2\text{O}_3$  has been investigated by thermoreflectance (TR) spectroscopy. Low-temperature TR spectra clearly show a series of band-edge excitons for  $c\text{-In}_2\text{O}_3$ . The threshold energy for the exciton series was determined. One transition feature of direct gap caused by BMS was detected in all TR spectra from 20 to 300 K. The Fermi-level ( $E_F$ ) energy above conduction-band edge ( $E_C$ ) is determined to be  $E_F - E_C \approx 92$  meV. The energy value causes a calculated electron density of  $\sim 2.1 \times 10^{19} \text{ cm}^{-3}$ . The direct gap of  $c\text{-In}_2\text{O}_3$  with BMS is 3.43 eV at 300 K. Free exciton, bound exciton complexes, donor–acceptor pair transition, and defect emissions have been evaluated by photoluminescence (PL) measurements from 10 to 300 K. Photoresistivity change (i.e.,  $5.71 \times 10^{-2} \rightarrow 4.85 \times 10^{-2} \Omega\text{-cm}$ ) under the illumination of halogen lamp ( $5 \text{ mW}\cdot\text{cm}^{-2}$ ) for  $c\text{-In}_2\text{O}_3$  thin-film nanorods was detected. The experimental results show  $\text{In}_2\text{O}_3$  nanocrystals an appropriate candidate applied not only for light-emitting devices but also for photoelectric-conversion cells.

Recently, transparent conducting oxide (TCO) represents itself as a crucial candidate for application in short-wavelength optoelectronics including transparent electric contacts and light emitting devices. Among the TCOs,  $\text{In}_2\text{O}_3$  nanomaterials receive considerable attentions in a variety of technological applications such as transparent thin-film transistors,<sup>1</sup> field-emission devices,<sup>2</sup> nanowire-based field-effect transistors,<sup>3–5</sup> transparent conductors,<sup>6</sup> ultraviolet (UV) sensors,<sup>7</sup> light-emitting devices,<sup>8</sup> photoelectrochemical devices,<sup>9</sup> and antireflection layer for Si solar cells.<sup>10</sup> To reach these goals, electronic structure and band-edge excitons are the key factors for determination of optoelectronic properties of  $\text{In}_2\text{O}_3$  nanocrystals.

$\text{In}_2\text{O}_3$  is a wide band gap semiconductor ( $>3$  eV) that can form different crystal structures of cubic  $\text{In}_2\text{O}_3$  ( $c\text{-In}_2\text{O}_3$ ),<sup>3,11–13</sup> hexagonal  $\text{In}_2\text{O}_3$  ( $h\text{-In}_2\text{O}_3$ ),<sup>14,15</sup> and rhombohedral  $\text{In}_2\text{O}_3$  ( $rh\text{-In}_2\text{O}_3$ ).<sup>16,17</sup> The  $c\text{-In}_2\text{O}_3$  is generally the main stable phase crystallized in body-centered cubic (bcc) structure with lattice constant  $a = 10.11 \text{ \AA}$  (space group  $Ia3$ ).<sup>14</sup> The  $h\text{-In}_2\text{O}_3$  belongs to a high-pressure modification, which is Corundum type with  $a = 5.49 \text{ \AA}$  and  $c = 14.52 \text{ \AA}$ , respectively. The crystalline phase of

$rh\text{-In}_2\text{O}_3$  may be obtained by annealing  $\text{InOOH}$  precursor at  $490^\circ\text{C}$  under atmosphere.<sup>16</sup> Its optical property showed slightly lower band gap than that of  $c\text{-In}_2\text{O}_3$ .<sup>18</sup> To evaluate band character of indium oxide, various experimental studies on electronic structure of  $c\text{-In}_2\text{O}_3$  using X-ray photoemission spectroscopy (XPS) have been reported.<sup>19,20</sup> The experimental results showed that  $c\text{-In}_2\text{O}_3$  nanomaterial is a degenerate semiconductor with its Fermi level ( $E_F$ ) higher above conduction-band edge ( $E_C$ ) to form Burstein–Moss shift (BMS).<sup>21</sup> The occurrence of BMS is owing to surface-electron accumulation layer and high-density oxygen vacancies ( $V_O$ ) that existed in the  $\text{In}_2\text{O}_3$ .<sup>18,22</sup> Because of the BMS effect, variety of characterization methods and different crystalline states in  $\text{In}_2\text{O}_3$  (thin films,<sup>23</sup> single crystal,<sup>24</sup> and nanostructures) discrepancies on reporting the values of band gap ranging from 2.9 to 3.75 eV were found.<sup>18,22–24</sup> For  $\text{In}_2\text{O}_3$ , most of the band gap values were obtained by transmittance or optical-absorption

Received: September 12, 2011

Revised: November 9, 2011

Published: November 10, 2011

measurements to date. Considerable error in estimating band gap via analyzing a long-section wavelength of absorption edge might occur. The BMS effect on the surface of  $\text{In}_2\text{O}_3$  nanorod should be considered, but the value of BMS (i.e.,  $E_F - E_C$ ) is difficult to measure directly by only transmittance or absorption measurements.

Experimental studies on excitons and electronic structure of nanocrystals are crucial and essential in chemical-physics field for semiconductor nanostructures.<sup>25–27</sup> Comprehensive evaluation of the origin for band-edge excitons and BMS in  $\text{In}_2\text{O}_3$  nanocrystals is very important. In this Article, we demonstrate thermoreflectance (TR) as an important tool to probe band-edge excitons and electronic structure of  $\text{In}_2\text{O}_3$  nanocrystals. TR is a powerful technique for probing direct transition in semiconductors and oxide nanostructures.<sup>28–30</sup> The derivative-like TR spectra suppress uninteresting background effects and emphasize the transition features localized in the energy region near direct critical-points transitions.<sup>31</sup> The transition energy can be determined accurately via spectral analysis of the derivative line shape of the TR feature. The  $c\text{-In}_2\text{O}_3$  nanowires were grown on Si (100) substrate using vapor transport driven by vapor–liquid–solid (VLS) mechanism. Low-temperature TR spectrum revealed an excitonic series containing  $E_1 = 3.398$  eV ( $n = 1$ ) and  $E_2 = 3.428$  eV ( $n = 2$ ) at 20 K. The direct gap (threshold energy) for the exciton series was hence determined to be 3.438 eV at 20 K. One additional transition feature  $E_{V\text{-CF}} = 3.53$  eV, which originates from the direct gap caused by BMS, has also been detected in the TR spectrum at 20 K. The energy of BMS is evaluated to be  $E_F - E_C \approx 92$  meV. The BMS results in an electron density (calculated) close to  $2.1 \times 10^{19} \text{ cm}^{-3}$ . Free exciton, bound exciton complexes (BECs), donor–acceptor pair (DAP) transition, and defect emissions have also been evaluated by temperature-dependent photoluminescence (PL) measurements for the  $c\text{-In}_2\text{O}_3$  nanorods. PL measurements of different laser powers were carried out to probe and identify the origins of below-band-edge transitions in the  $\text{In}_2\text{O}_3$  nanowires. On the basis of the experimental analysis, the below- and above-band-edge structures of  $c\text{-In}_2\text{O}_3$  thin-film nanowires are realized.

Figure 1a shows the top view of field-emission scanning electron microscope (FESEM) image of the as-grown  $\text{In}_2\text{O}_3$  thin-film nanowires. Figure 1b reveals cross-section view of the thin-film nanowires. From Figure 1a,b, high density and highly compact  $\text{In}_2\text{O}_3$  nanorods have been successfully grown on Si substrate. Figure 1b also shows that the  $\text{In}_2\text{O}_3$  thin-film nanorods consisted of a compact continuous film ( $\sim 200$  nm) initially deposited on Si (100) substrate; then, most of the individual nanowires were grown on the continuous film approximately vertical to the substrate plane. As shown in Figure 1a, many of the nanowires demonstrate a tapered tip for each individual nanorod in which four apparent  $\{111\}$  faces are usually consisted in the wire tip due to different surface energies affect the growth rate of different crystalline planes.<sup>32</sup> The tapered wire tip with four equivalent  $\{111\}$  faces of  $\text{In}_2\text{O}_3$  also confirms cubic crystalline phase of the  $\text{In}_2\text{O}_3$  nanowires (i.e.,  $c\text{-In}_2\text{O}_3$ ). Because of different nucleation mechanisms, surface energies, and growth rates in cubic indium oxide, the  $c\text{-In}_2\text{O}_3$  nanostructures can form different possible shapes of arrow-like nanorods,<sup>33,34</sup> nanotowers,<sup>32,35</sup> and octahedrons.<sup>36</sup> The outline shapes for these nanostructures are also demonstrated in Figure 1c for comparison. In general, for  $c\text{-In}_2\text{O}_3$  with a bcc structure, the relationship between the surface formation energies should be corresponding to  $\gamma_{\{111\}} < \gamma_{\{100\}} < \gamma_{\{110\}}$ . Therefore, the highest growth rate must occur in the crystal direction of  $\langle 110 \rangle$ , the second is  $\langle 100 \rangle$ , and finally the

slowest is  $\langle 111 \rangle$ . This result is why each nanowire tip usually presents four apparent  $\{111\}$  faces, and the  $c\text{-In}_2\text{O}_3$  easily forms a stacking formula of nanotower with each tower edge along the highest growth rate of  $\{110\}$  plane. Figure 1d,e displays the transmission electron microscope (TEM) images of a single  $c\text{-In}_2\text{O}_3$  nanowire with a tapered tip on the wire end. The growth direction of the 1D  $c\text{-In}_2\text{O}_3$  nanowire was along  $\langle 100 \rangle$ . The length and diameter for the nanowires in Figures 1d,e are around 0.9 to 1  $\mu\text{m}$  and 80–120 nm, respectively. As shown in Figure 1a, d,e, the tapered tips and tower edges are usually the easily forming structures for the  $c\text{-In}_2\text{O}_3$  nanorods. The drawing in Figure 1d shows that the tip angle for the tapered nanorod is  $70^\circ$  and that of the tower edge is  $\sim 110^\circ$ . Because the VLS catalytic growth of the individual  $c\text{-In}_2\text{O}_3$  nanowire using Au, the gold nanoparticle catalysis was usually encapsulated inside the wire end.<sup>37</sup> It was evident in Figure 1d. This situation can be seen more clearly in the TEM image of Figure 1f that is enlarged from the (f) region in Figure 1e. The ascending of gold nanoparticle droplet to the wire end verifies the VLS growth of the individual  $c\text{-In}_2\text{O}_3$  nanowire. Figure 1f also indicates that a series of stacking (01 $\bar{1}$ ) planes construct the nanowire along the  $\langle 100 \rangle$  direction. It can be seen more clearly from the high-resolution transmission electron microscope (HRTEM) images in Figure 1g,h. Figure 1g–i are magnified from a center box in Figure 1e. The interplanar spacings of  $d_{(01\bar{1})}$  and  $d_{(200)}$  were determined to be 0.715 and 0.505 nm, which matched well with the cubic structure of  $\text{In}_2\text{O}_3$ . The selected-area electron diffraction (SAED) pattern in Figure 1i also confirms the cubic crystalline phase of the  $c\text{-In}_2\text{O}_3$  tapered nanorods.

To probe clearly the near-band-edge electronic structure of  $c\text{-In}_2\text{O}_3$  nanorods, we implemented low-temperature TR measurement at 20 K. The TR measurement can keep uniformity of periodically thermal modulation of each nanowire to result in easily resolved derivative line-shape spectrum for  $c\text{-In}_2\text{O}_3$ .<sup>38</sup> Displayed in Figure 2 by the dashed line is the TR spectrum of  $c\text{-In}_2\text{O}_3$  at 20 K together with three PL spectra excited with different excitation powers. The derivative line shape of TR spectrum in Figure 2 clearly shows five interband transition features denoted as BX,  $E_1$ ,  $E_2$ ,  $E_{A\text{-CF}}$ , and  $E_{V\text{-CF}}$ . The solid line for the TR spectrum is the least-squares fit by using a first derivative Lorentzian line-shape function appropriate for excitonic transition expressed as<sup>30,39</sup>

$$\frac{\Delta R}{R} = \text{Re} \left[ \sum_{i=1}^n A_i e^{j\phi_i} (E - E_i + j\Gamma_i)^{-2} \right] \quad (1)$$

where  $i$  is the respective transition,  $A_i$  and  $\phi_i$  are amplitude and phase of the line shape, and  $E_i$  and  $\Gamma_i$  are the energy and broadening parameter for each interband transition in  $c\text{-In}_2\text{O}_3$ . The fit yields transition energies that are respectively indicated by arrows in Figure 2. The obtained transition energies are BX = 3.362 eV,  $E_1 = 3.398$  eV,  $E_2 = 3.428$  eV,  $E_{A\text{-CF}} = 3.468$  eV, and  $E_{V\text{-CF}} = 3.53$  eV at 20 K, respectively. The BX is closely related to a transition caused by BECs in  $c\text{-In}_2\text{O}_3$  nanorods and which will be discussed later together with PL measurements. The  $E_1$  and  $E_2$  features belong to the band-edge excitonic series in  $c\text{-In}_2\text{O}_3$  nanostructures. Previous density-of-states calculations of  $c\text{-In}_2\text{O}_3$  showed that the valence-band edge ( $E_V$ ) is dominated by O 2p states, whereas the  $E_C$  edge originates from In 5s orbitals.<sup>40</sup> The transition energies of the exciton sequence ( $E_1$  and  $E_2$ ) can be further analyzed by using Rydberg series

$$E_n = E_{n=\infty} - \frac{R_{yd}}{n^2}, \quad n = 1, 2, 3, \dots \quad (2)$$

## *c*-In<sub>2</sub>O<sub>3</sub> tapered nanorods

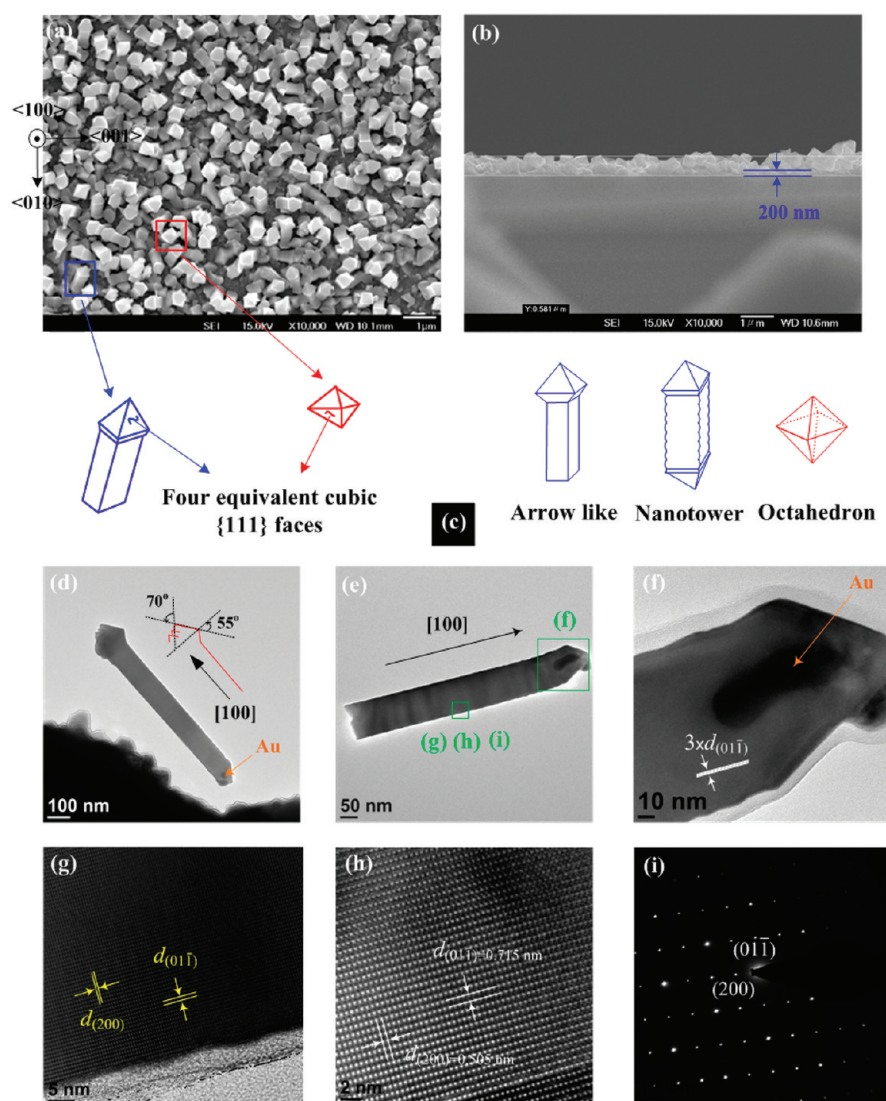


**Figure 1.** FESEM images of (a) top view and (b) cross-section view for as-grown In<sub>2</sub>O<sub>3</sub> nanorods. (c) Four equivalent {111} faces presented on the top of tapered nanorods. The possible shapes for the *c*-In<sub>2</sub>O<sub>3</sub> nanostructures are also displayed. (d–f) TEM images for a single *c*-In<sub>2</sub>O<sub>3</sub> nanorod along the [100] direction. (g–h) HRTEM images of *c*-In<sub>2</sub>O<sub>3</sub>. The interplanar distances of  $d_{(011)}$  and  $d_{(200)}$  are indicated. (i) SAED pattern of *c*-In<sub>2</sub>O<sub>3</sub> nanorod.

where  $R_{yd}$  is the effective Rydberg constant,  $n$  is principal quantum number, and  $E_{n=\infty}$  is the threshold energy for the exciton series. From the analysis, the exciton binding energy for  $n = 1$  ground-state level (i.e.,  $R_{yd}$ ) is  $\sim 40$  meV. The threshold energy (i.e., direct gap) for the *c*-In<sub>2</sub>O<sub>3</sub> nanorods is  $E_g^d = 3.438$  eV at 20 K. The transition features of  $E_{A-CF}$  and  $E_{V-CF}$  in Figure 2 are, respectively, assigned to be the transitions of acceptor to  $E_C$  and  $E_V$  to  $E_C$  by taking into account the BMS effect. The origins of  $E_{A-CF}$  and  $E_{V-CF}$  will be identified and discussed later via the analyses of polarized TR (PTR), temperature-dependent PL, and temperature-dependent resistivity measurements.

As shown in Figure 2, for characterization of the below-band-edge transitions in *c*-In<sub>2</sub>O<sub>3</sub> nanowires, three high-resolution PL spectra obtained by different excitation sources of 325 nm/33 mW·cm<sup>-2</sup> (denoted as 325 nm-Lo), 266 nm/2.4 W·cm<sup>-2</sup> (denoted as 266 nm-Lo), and 266 nm/24 W·cm<sup>-2</sup> (denoted as 266 nm-Hi) have been demonstrated at 20 K. The purpose of

changing different excitation power is to excite and identify clearly various excitonic and defect emissions observed in *c*-In<sub>2</sub>O<sub>3</sub> nanowires. There are many emission features observed in the PL spectra excited with different laser powers, including free exciton (FX = 3.378 eV), BECs (A = 3.368 eV, B = 3.360 eV, and C = 3.353 eV), DAP, A-LO (3.297 eV), B-LO (3.289 eV), and DAP-LO at 20 K. The energy of DAP emission is closely related to the DAP's distance  $r$  in Coulombic energy expressed as:  $E_{DAP} = E_g - E_D - E_A + e^2/(4\pi\epsilon r)$ , where  $E_D$  and  $E_A$  are the binding energies of donor and acceptor,  $e$  is the electron charge, and  $\epsilon$  is the permittivity of the material. With the increase in excitation power, the photoexcited DAPs become high density; then, the average distance  $r$  shortened to increase photon energy. From Figure 2, the energies of DAP are, respectively, 3.308, 3.311, and 3.315 eV by increasing excitation powers from 325 nm-Lo, to 266 nm-Lo, to 266 nm-Hi. The inset in Figure 2 also shows high-resolution PL spectrum excited by 266 nm-Hi at 10 K. The condition of high-power



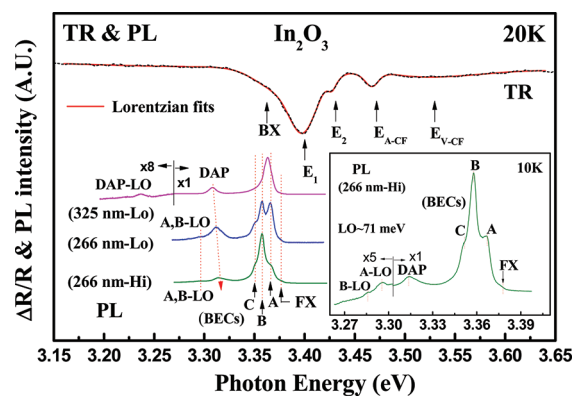


**Figure 2.** Experimental TR and PL spectra of *c*-In<sub>2</sub>O<sub>3</sub> thin-film nanorods at 20 K. The three PL spectra were excited by different laser powers of 325 nm-Lo (33 mW·cm<sup>-2</sup>), 266 nm-Lo (2.4 W·cm<sup>-2</sup>), and 266 nm-Hi (24 W·cm<sup>-2</sup>). The inset depicts the low-temperature PL spectrum at 10 K for showing clearly the emission features below band edge.

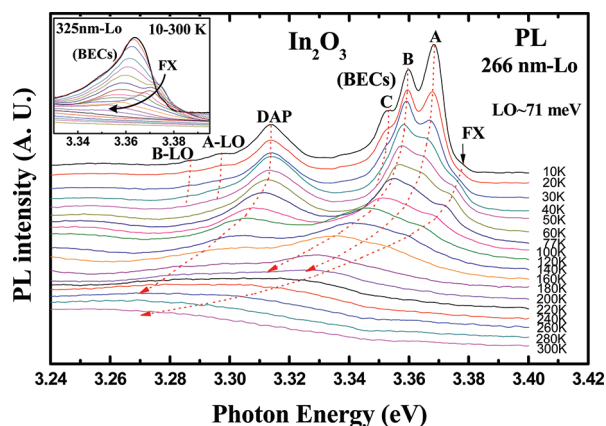


**Figure 3.** Temperature-dependent PL spectra of *c*-In<sub>2</sub>O<sub>3</sub> nanorods between 10 and 300 K excited by 266 nm-Lo. The inset shows the temperature-dependent PL spectra of 10–300 K excited by 325 nm-Lo.

and low-temperature enhances more clearly the FX peak as well as the longitudinal optical (LO) phonon replicas of the BECs (i.e., A-LO and B-LO). The energy of LO phonon obtained by PL is  $\sim 71$  meV similar to the previous reported values.<sup>24,41</sup> The energy of the first-order LO replica of DAP (DAP-LO) excited by 325 nm-Lo is 3.237 eV observed in Figure 2. The comparison of TR and PL spectra in Figure 2 shows that the energy difference between  $E_1$  and FX is  $\sim 20$  meV at 20 K. The energy difference between the ground-state level ( $n = 1$ ) and free exciton is due to the exciton–photon interaction that scattered inelastically by phonons (i.e., exciton–polariton) in nanocrystals.<sup>42</sup> When higher-energy photons absorbed by the *c*-In<sub>2</sub>O<sub>3</sub> thin-film nanorods, the inelastic scattering event by phonons will eventually render the polaritons exiting the sample with emission in lower-energy photons (i.e.,  $FX = E_1 - E_{\text{phonon}}$ ).

To verify the origins of below-band-edge transitions in *c*-In<sub>2</sub>O<sub>3</sub> thin-film nanorods, we carried out temperature-dependent PL measurements. Figure 3 shows the PL spectra of *c*-In<sub>2</sub>O<sub>3</sub> nanorods from 10 to 300 K obtained by 266 nm-Lo excitation condition. Many of the below band-edge emission features including

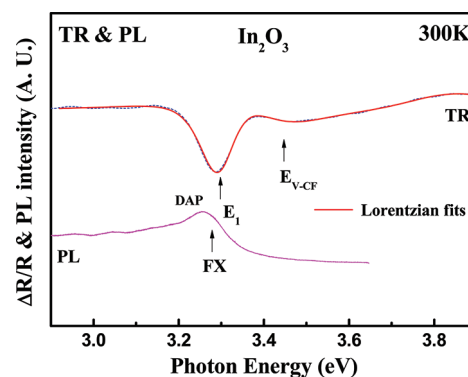


**Figure 4.** Room-temperature TR and PL spectra of *c*-In<sub>2</sub>O<sub>3</sub> nanorods.

FX, A, B, C, DAP, A-LO, and B-LO can be detected in the low-temperature PL spectra. The FX feature near 3.378 eV at 10 K is inferred to be a free-exciton luminescence. This assignment can be verified from the fact that the temperature dependence of peak intensity of FX decreases more slowly than that of the other features A, B, and C when the temperature increases. The inset in Figure 3 shows more clearly that the BECs followed by FX and the FX peak will eventually dominate the emission feature at higher temperatures from 10 to 300 K under the excitation condition of 325 nm-Lo. As shown in Figure 3, the emission peaks of  $A \approx 3.368$  eV,  $B \approx 3.360$  eV, and  $C \approx 3.353$  eV at low temperature are inferred to be the BECs, each peak bounded to a neutral donor level by oxygen vacancy ( $V_O$ ) to form a  $D^0X$  feature similar to that in CdS nanobelts.<sup>25</sup> The oxygen vacancies in *c*-In<sub>2</sub>O<sub>3</sub> are a series of shallow donor levels (defects) near the surface of nanorod to contribute conductivity.<sup>43</sup> The appearance of multiple bound-exciton peaks A, B, and C in Figure 3 implies that oxygen vacancies in *c*-In<sub>2</sub>O<sub>3</sub> nanorods may probably be a series of shallow donor levels similar to a defect donor band that existed in Ga<sub>2</sub>O<sub>3</sub> nanostructures constructed by  $V_O$ .<sup>44</sup> As observed in Figure 3, when the temperature increases, the shallow donor levels ionized rapidly to decrease and broaden the PL features of the BECs. The A, B, and C peaks are free from the defect donors' bounding, and they will finally merge with the FX peak at even higher temperatures. The DAP feature is a donor–acceptor pair emission that presents a red-shift behavior similar to the BECs features. The acceptors in DAP might be indium–oxygen vacancy pairs  $V_O-V_{In}$ , and the donors are the oxygen vacancies  $V_O$ . For the VLS growth, when the indium oxide nanocrystallite forms, the InO<sub>1-x</sub> molecules are easy to volatilize at high temperature. The consequence is easy to form oxygen vacancies, indium vacancies, and oxygen–indium vacancy pairs<sup>45</sup> in the In<sub>2</sub>O<sub>3</sub> nanostructures. As shown in Figure 3, the relative intensity of the DAP decreased slowly before 100 K and reduced quickly when the temperature increased up to 260 K. With  $T > 260$  K, the DAP is shown to be approximately weaker and broadened to merge with the free exciton peak FX. When photons emitted out from the *c*-In<sub>2</sub>O<sub>3</sub> nanorods, the FX peak closely relates to the band-edge emission, and DAP correlates with the recombination of donors and acceptors. The binding energy of  $E_D + E_A$  can be approximately estimated from the low-temperature PL spectrum at 10 K by  $FX-DAP \approx 0.068$  eV. (See Figure 3.) If the Coulombic energy is neglected and the binding energy of  $E_D$  is estimated to be  $\sim 6$  meV (i.e., ionization temperature of A peak is around 60–77 K), the binding energy of  $E_A$  is estimated to be 62 meV.

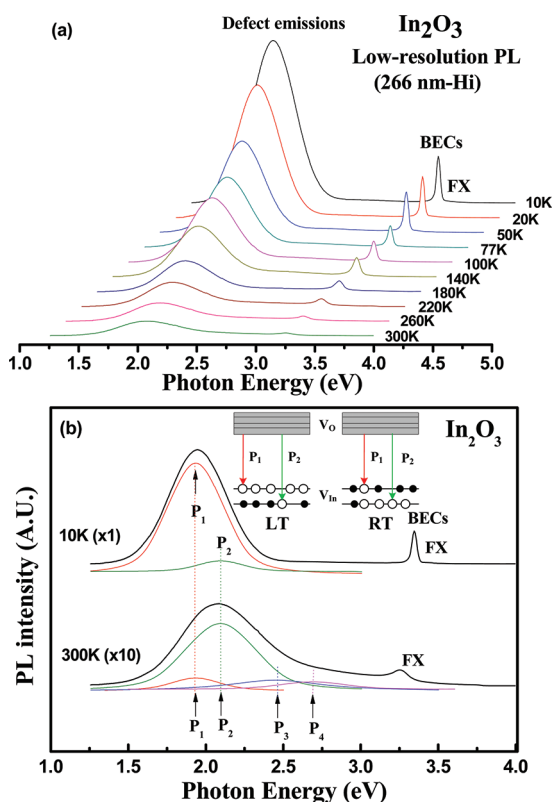


**Figure 5.** (a) Temperature-dependent PL spectra of *c*-In<sub>2</sub>O<sub>3</sub> nanorods between 10 and 300 K excited by 266 nm-Hi. (b) PL spectra of 10 and 300 K together with the defect emission mechanisms for shallow donor ( $V_O$ ) and deeper acceptor ( $V_{In}$ ) at room temperature (RT) and low temperature (LT) are depicted in the inset for comparison.

Figure 4 shows the room-temperature TR and PL spectra of the *c*-In<sub>2</sub>O<sub>3</sub> thin-film nanowires. In comparison with the low-temperature TR spectrum in Figure 2 ( $T = 20$  K), only two transition features of  $E_1$  and  $E_{V-CF}$  are detected at 300 K. The BX,  $E_2$ , and  $E_{A-CF}$  features are weaker and not clearly detected in Figure 4 due to thermal effect. The transition energies obtained from the line-shape fitting using eq 1 are  $E_1 = 3.298$  eV and  $E_{V-CF} = 3.43$  eV, respectively. The  $E_{V-CF}$  feature is the direct band gap by taking into account BMS in *c*-In<sub>2</sub>O<sub>3</sub> thin-film nanowires. The energy value  $E_{V-CF} = 3.43$  eV agrees well with the center wavelength of the absorption edge (355–365 nm) observed in previous transmittance spectra of degenerate In<sub>2</sub>O<sub>3</sub> thin films.<sup>46</sup> It sustains that the determination of band gap of *c*-In<sub>2</sub>O<sub>3</sub> is equal to  $E_{V-CF}$ . For the room-temperature PL spectrum shown in Figure 4, a broadened peak combining DAP and FX is present. The energy of FX is 3.278 eV at 300 K. It is lower than  $E_1$  by a phonon energy  $\sim 20$  meV, similar to those observed in Figure 2 at 20 K.

To investigate below band-edge imperfection states in *c*-In<sub>2</sub>O<sub>3</sub>, we carried out PL measurements with lower resolution in a wide energy range from 1.25 to 4 eV. The excitation condition of laser power is 266 nm-Hi. Figure 5a shows the temperature-dependent PL spectra of *c*-In<sub>2</sub>O<sub>3</sub> nanorods in the temperature range between 10 and 300 K. Beside the main exciton peak (BECs and FX), one prominent defect-related emission was observed in the PL spectra near 2 eV. With increasing temperatures, the PL intensities for both exciton peak and defect emission are simultaneously decreased. The energy positions of the exciton peak demonstrate an energy red-shift behavior with the increase

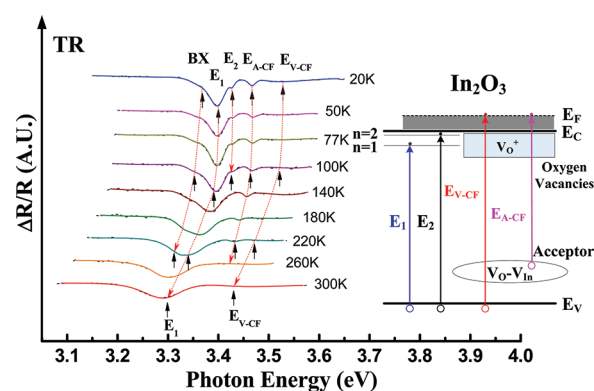


**Figure 6.** Temperature-dependent TR spectra of *c*-In<sub>2</sub>O<sub>3</sub> thin-film nanorods between 20 and 300 K. The inset shows the possible band-edge scheme for the *c*-In<sub>2</sub>O<sub>3</sub> nanorods by taking into account band-edge excitons, defects, and Burstein–Moss shift.

in temperatures from 10 to 300 K, whereas the defect emission peak seems to be blue shift due to many of the defect luminescences that consisted of one defect emission feature. This situation can be evident in Figure 5b. The defect emissions below band edge of *c*-In<sub>2</sub>O<sub>3</sub> nanorods may come from the recombinations of donors and acceptors. The donors may be a series of shallow  $V_O$  levels, and the acceptors include shallow  $V_O-V_{In}$  pairs and deeper indium vacancies  $V_{In}$ . As shown in the room-temperature PL spectrum in Figure 5b, at least four Gaussian peaks denoted as  $P_1$  ( $\sim 1.935$  eV),  $P_2$  ( $\sim 2.095$  eV),  $P_3$  ( $\sim 2.45$  eV), and  $P_4$  ( $\sim 2.69$  eV) can be used to fit in defect emission peaks of the *c*-In<sub>2</sub>O<sub>3</sub> nanorods. The energy positions of  $P_3$  and  $P_4$  are similar to previous PL peaks of In<sub>2</sub>O<sub>3</sub>.<sup>41,47</sup> The energies of  $P_1$  and  $P_2$  are lower than those of  $P_3$  and  $P_4$ . The  $P_1$  and  $P_2$  emissions are, respectively, inferred to come from the lowest  $V_O$  level to the acceptor levels of higher  $V_{In}$  and lower  $V_{In}$ , as shown in the inset in Figure 5b. At low temperatures, the higher  $V_{In}$  acceptor level is nearly empty, but the lower  $V_{In}$  level is almost occupied by electron to render strong  $P_1$  and lower  $P_2$  intensities. When the temperature increases, thermal ionization effect between the higher  $V_{In}$  and lower  $V_{In}$  acceptor levels causes the  $P_1$  to decrease but the  $P_2$  to be enhanced, as shown in the PL results and inset in Figure 5b.

Temperature-dependent TR spectra of *c*-In<sub>2</sub>O<sub>3</sub> nanorods in the temperature range between 20 and 300 K are shown in Figure 6. The transition energies obtained by the Lorentzian line-shape fits using eq 1 are indicated with arrows, and their temperature-variation traces are depicted with dotted lines. All transition features demonstrate an energy red-shift behavior and a line-shape broadened character with the increase in temperatures from 20 to 300 K such as the general semiconductor behavior. The bound exciton (BX) feature in the TR spectra in Figure 6 agrees well with the average energy position of the BECs peaks presented in the temperature-dependent PL spectra in Figure 3. The  $E_1$  and  $E_2$  features are band-edge excitons of ground state ( $n = 1$ ) and the first excited state ( $n = 2$ ), which show an effective Rydberg constant of 40 meV ( $R_{yd}$ ) and a direct gap of 3.438 eV ( $E_g^d$ ) at 20 K (Figure 2). The binding energy of  $n = 2$  level ( $E_2$ ) was estimated to be  $\sim 10$  meV using eq 2. The value is in good accordance with the ionization temperature of  $E_2$  with  $T > 100$  K, as shown in temperature-dependent TR spectra in Figure 6. The energy of the  $E_{A-CF}$  transition is 3.468 eV at 20 K, which lies in between  $E_g^d$  and  $E_{V-CF}$  (3.53 eV). The inset in Figure 6 depicts a band diagram for the indication of band-edge

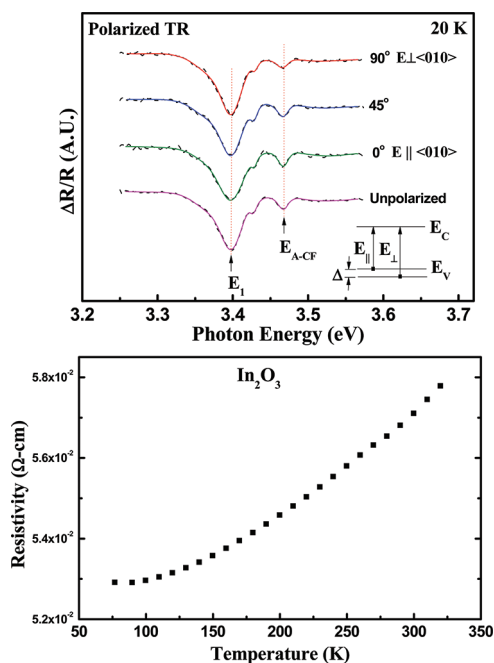


**Figure 7.** PTR spectra of *c*-In<sub>2</sub>O<sub>3</sub> used for verification of the transition origin of the  $E_{A-CF}$  feature. The lower part is temperature dependence of resistivities of *c*-In<sub>2</sub>O<sub>3</sub> degenerate semiconducting-oxide nanorods.

transitions in *c*-In<sub>2</sub>O<sub>3</sub> nanorods. There are two electronic effects of BMS, and shallow  $V_O-V_{In}$  pairs contributed to the occurrence of the  $E_{A-CF}$  transition. The  $E_{A-CF}$  transition is inferred not coming from the crystal-field-splitting band ( $\Delta$ ) in the  $E_V$  of *c*-In<sub>2</sub>O<sub>3</sub>. This inference is evident in the upper part of Figure 7, where PTR spectra of the *c*-In<sub>2</sub>O<sub>3</sub> thin-film nanorods with different polarization angles of 0 (i.e.,  $E \parallel \langle 010 \rangle$ ) as the direction indicated in Figure 1a), 45°, and 90° (i.e.,  $E \perp \langle 010 \rangle$ ) are present. The relative intensities of  $E_1$  and  $E_{A-CF}$  transitions measured by PTR are nearly invariant. It verifies that the  $E_{A-CF}$  transition is not originated from the valence-band splitting, followed by selection rule. The  $E_{A-CF}$  is closely related to the transition from shallow acceptor level of  $V_O-V_{In}$  pair to the  $E_F$  above  $E_C$ . The temperature-variation behavior of the  $E_{A-CF}$  feature in Figure 6 shows that the amplitude of  $E_{A-CF}$  becomes smaller and broadened with temperatures up to 260 K, similar to the temperature dependence of DAP presented in Figure 3. This phenomenon sustains the assignment of transition origin of  $E_{A-CF}$ . Furthermore, the energy difference between  $E_{V-CF}$  and  $E_{A-CF}$  is 62 meV at 20 K, which also matches well with the acceptor binding energy  $E_A$  (in DAP) obtained by PL in Figure 3. This result verifies that the  $E_{A-CF}$  comes from the transition of  $V_O-V_{In}$  pairs to the  $E_F$  above  $E_C$ .

To verify the BMS effect in the *c*-In<sub>2</sub>O<sub>3</sub> thin-film nanorods, temperature-dependent resistivity measurement from 77 to 320 K was carried out. Displayed in the lower part of Figure 7 is the temperature dependence of resistivities of *c*-In<sub>2</sub>O<sub>3</sub> thin-film nanorods. For a degenerate semiconductor with BMS, the dependence of resistivity may present a metallic behavior owing to the fact that the  $E_C$  bottom always fills with electrons. The temperature dependence of resistivities of *c*-In<sub>2</sub>O<sub>3</sub> shows that resistivity increases with the increase in temperatures. The experimental evidence reveals that *c*-In<sub>2</sub>O<sub>3</sub> is a degenerate semiconductor with its Fermi level higher above conduction-band edge (i.e.,  $E_F > E_C$ ). The energy difference between  $E_{V-CF}$  and  $E_g^d$

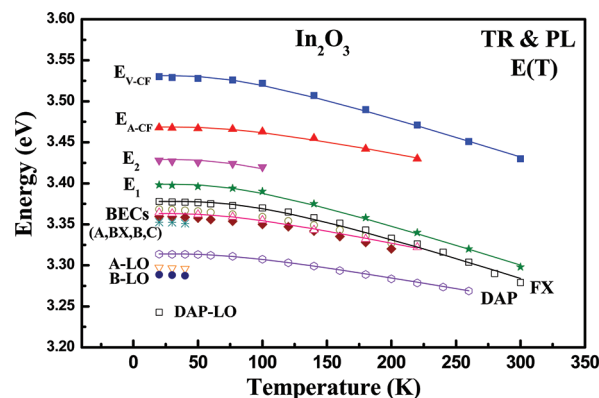


**Figure 8.** Temperature dependences of transition energies of *c*-In<sub>2</sub>O<sub>3</sub> nanorods obtained by TR and PL measurements.

**Table 1.** Values of Fitting Parameters of Bose–Einstein Type Equation  $E_{iB}(T) = E_{iB}(0) - \varepsilon_{iB}/[\exp(\hbar\omega_{iB}/kT) - 1]$ , Which Describe Temperature Dependences of Transition Energies of  $E_{V-CF}$ ,  $E_{A-CF}$ ,  $E_2$ ,  $E_1$ , BX, FX, and DAP Features Obtained by TR and PL Measurements

feature	$E_B(0)$ (eV)	$\varepsilon_B$ (meV)	$\hbar\omega_B$ (meV)
$E_{V-CF}$	$3.532 \pm 0.001$	$115 \pm 16$	$20 \pm 2$
$E_{A-CF}$	$3.469 \pm 0.001$	$70 \pm 12$	$20 \pm 2$
$E_2$	$3.429 \pm 0.001$	$117 \pm 16$	$20 \pm 2$
$E_1$	$3.399 \pm 0.001$	$115 \pm 17$	$20 \pm 2$
BX	$3.364 \pm 0.001$	$68 \pm 11$	$20 \pm 2$
FX	$3.378 \pm 0.001$	$120 \pm 20$	$22 \pm 4$
DAP	$3.311 \pm 0.001$	$70 \pm 10$	$21 \pm 2$

determines the value of BMS (i.e.,  $E_F - E_C = E_{V-CF} - E_g^d$ ). The value is  $\sim 92$  meV at 20 K. As the temperature increases, the  $E_1$  and  $E_{V-CF}$  transitions show nearly parallel temperature dependence from 20 to 300 K. (See Figure 6.) It means that  $E_F - E_C$  is also near 92 meV at 300 K. The relationship between carrier concentration ( $n_e$ ) and BMS ( $\Delta E$ ) is

$$\Delta E = E_F - E_C = \frac{\hbar^2}{2 \cdot m^*} \cdot (3\pi^2 \cdot n_e)^{2/3} \quad (3)$$

where  $m^*$  is the effective mass of electron. By taking into account the effective mass of  $m^* = 0.3m_0$ <sup>48,49</sup> in eq 3, the electron density by BMS ( $\Delta E = 92$  meV) can be calculated to be  $n_e = 2.1 \times 10^{19} \text{ cm}^{-3}$ . This value is comparable to the experimental value of  $2.2 \times 10^{19} \text{ cm}^{-3}$  for the *c*-In<sub>2</sub>O<sub>3</sub> thin film obtained by Hall-effect measurement. The resistivity of *c*-In<sub>2</sub>O<sub>3</sub> in Figure 7 is  $5.71 \times 10^{-2} \text{ } \Omega\text{-cm}$  at 300 K. The mobility can be determined to be  $4.8 \text{ cm}^2/\text{V}\cdot\text{sec}$ . The values of resistivity, electron concentration, and Hall mobility are in reasonable agreement with previous results obtained by undoped-degenerate *c*-In<sub>2</sub>O<sub>3</sub> thin-film nanostructures.<sup>46,50</sup>

Temperature dependences of transition energies above and below band edge in *c*-In<sub>2</sub>O<sub>3</sub> nanorods are depicted in Figure 8. The solid lines are fitted to a Bose–Einstein expression  $E_{iB}(T) = E_{iB}(0) - \varepsilon_{iB}/[\exp(\hbar\omega_{iB}/kT) - 1]$ , where  $i$  is the respective transition feature,  $\varepsilon_{iB}$  represents the strength of electron–phonon interaction, and  $\hbar\omega_{iB}$  corresponds to average phonon energy. The fitted results are listed in Table 1 for comparison. The obtained



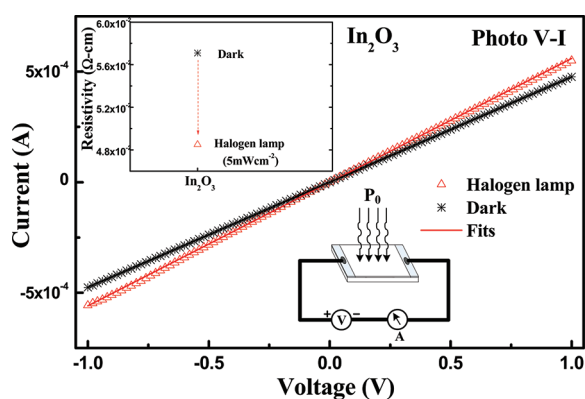


**Figure 9.** Photo  $V$ – $I$  curves of  $c$ - $\text{In}_2\text{O}_3$  thin-film photoconductor under illumination of halogen lamp (power density around  $5\text{ mW}\cdot\text{cm}^{-2}$ ) and under dark condition. The lower inset depicts measurement configuration of photo  $V$ – $I$ , and the upper part shows the photoresistivity change under light illumination.

values of  $\varepsilon_{\text{B}}$  (strength of electron–phonon interaction) are similar (i.e., 115–120 meV) for the transitions of  $E_{\text{V-CF}}$ ,  $E_2$ ,  $E_1$ , and FX due to the fact that they are band-to-band transitions across band gap to present nearly parallel temperature dependence of energy shift. (See Figure 8.) The defect-related transitions  $E_{\text{A-CF}}$ , BX (BECs), and DAP reveal smaller values of  $\varepsilon_{\text{B}}$  (i.e., 68–70 meV) in comparison with those of the band-to-band transitions. The temperature-insensitive energy shift is a general character for a defect transition with dangling bond or interstitial. The value of average phonon energy  $\hbar\omega_{\text{B}}$  for all transition features in  $c$ - $\text{In}_2\text{O}_3$  is 20–22 meV, which agrees well with the energy difference between  $E_1$  and FX induced by phonons. (See Figure 2.)

To study photoelectric conversion behavior of the highly conductive  $c$ - $\text{In}_2\text{O}_3$  thin-film nanorods, we carried out photo-voltage–current (photo  $V$ – $I$ ) measurement of the thin film at 300 K. The lower inset in Figure 9 shows the measurement setup of photo  $V$ – $I$  measurement for  $c$ - $\text{In}_2\text{O}_3$  photoconductor. Figure 9 depicts the photo  $V$ – $I$  curves under dark condition as well as under illumination of halogen lamp. The average power density of the halogen lamp illuminated on  $c$ - $\text{In}_2\text{O}_3$  is  $5\text{ mW}\cdot\text{cm}^{-2}$ . The scanning voltage range was from  $-1.0$  to  $1.0$  V. A nearly linear relation for the photoconductor with different illumination condition is present. The solid lines are the least-squares fits of an expression  $I = I_0 + GV$  to the photo  $V$ – $I$  data, where  $G$  is the photoconductance (A/V). The obtained values of photoconductance are  $G = 5.6 \times 10^{-4}$  (A/V) with halogen lamp and  $G = 4.7 \times 10^{-4}$  (A/V) under dark condition. The results render a photoresistivity change from  $(5.71 \text{ to } 4.85) \times 10^{-2}\ \Omega\cdot\text{cm}$ , as shown in the upper inset of Figure 9. Although the degenerate semiconducting-oxide nanorods present high conductivity, a considerable photoelectric-conversion yield still exists in  $c$ - $\text{In}_2\text{O}_3$  thin-film nanorods to present photoconductivity change. This property renders indium oxide nanostructure as an excellent candidate not only for TCO electronics but also as a window layer on solar-energy material to facilitate photoelectric conversion of the solar-cell structure.

In conclusion, a comprehensive study for whole below- and above-band-edge transitions in  $c$ - $\text{In}_2\text{O}_3$  thin-film nanowires has been explored. Direct optical observation of band-edge excitons and BMS by TR spectroscopy has been successfully carried out. The energy of band-edge exciton  $E_1$  is 3.298 eV at room temperature, and the direct gap is 3.43 eV with a BMS of  $\sim 92$  meV to

render an electron density approaching  $2.1 \times 10^{19}\text{ cm}^{-3}$ . Excitonic binding energies of 40 meV for  $E_1$  and 10 meV for  $E_2$  for an exciton series can be observed by temperature-dependent TR measurements of  $c$ - $\text{In}_2\text{O}_3$ . The threshold energy for the Rydberg series is 3.338 eV at 300 K. Power-dependent and temperature-dependent PL measurements verify and identify the properties of below-band-edge transitions including free exciton, BECs, DAPs, LO phonon replicas, and defect emissions. Photo  $V$ – $I$  measurements show well-behaved photoelectric conversion for the  $c$ - $\text{In}_2\text{O}_3$  thin-film photoconductor. On the basis of the experimental analyses, physical-chemistry behaviors of the indium oxide nanowires are realized, and their potential applications are manifested.

## EXPERIMENTAL METHODS

**Nanowire Growth.** The  $\text{In}_2\text{O}_3$  nanowires were grown using vapor transport driven by VLS mechanism.<sup>51</sup> A horizontal tube furnace was utilized for the growth. Molten indium (0.5 g, 99.9999%) was the source material and put into a boat placed at the center of the quartz tube. A thin layer of gold (5 nm) was predeposited on silicon (001) substrates by sputtering. The substrates were placed in another boat and positioned downstream. The quartz tube was evacuated and the furnace was heated to 900 °C with a rate of 10 °C/min. Highly pure oxygen carried by argon gas was fed into the quartz tube. The growth temperature was 650 °C with a background pressure of 0.5 Torr. Typical growth time was 2 h. After the growth, samples were then cooled under the same ambient gas. The chemical reaction for the growth process was  $4\text{In}_{(\text{g})} + 3\text{O}_{2(\text{g})} \rightarrow 2\text{In}_2\text{O}_{3(\text{s})}$ .

**Characterization.** The TR experiments of the  $c$ - $\text{In}_2\text{O}_3$  thin-film nanowires were implemented using indirect heating manner with a gold-evaporated quartz plate as the heating element.<sup>30,52,53</sup> The thin sheet-type sample was closely attached on the heating element by silicone grease. The on–off heating disturbance uniformly modulated the individual nanorods periodically. An 150 W xenon-arc lamp filtered by a PTI 0.2 m monochromator provided the monochromatic light. The incident light was focusing onto the sample with a spot size of  $\sim 100\ \mu\text{m}^2$ . The reflected and scattering lights from the thin-film nanorods were collected and detected by a Hamamatsu H3177-51 PMT module. The signal was detected and recorded via an EG&G model 7265 lock-in amplifier and a personal computer. A closed-cycle cryogenic refrigerator with a thermometer controller facilitated the temperature-dependent measurements. High-resolution PL measurements were carried out in a spectral measurement system where an iHR 550 imaging spectrometer equipped with a 2400 grooves/mm grating acted as the optical dispersion unit. The low-resolution PL spectra were detected by a QE65000 spectrometer. The CCD array detections were employed in the PL measurements. The pumping light sources are a Q-switched diode-pumped solid-state laser ( $\lambda = 266\text{ nm}$ ) and a helium–cadmium laser ( $\lambda = 325\text{ nm}$ ). A set of neutral density filters changed and controlled the pumping powers of the lasers. Photo  $V$ – $I$  measurements were carried out using a tungsten halogen lamp as the white-light source. The  $c$ - $\text{In}_2\text{O}_3/\text{Si}$  sample was cut into a rectangular shape with dimension of  $\sim 0.4 \times 0.3\text{ cm}^2$  in area. The two ends of the specimen were coated with In as the ohmic-contact electrodes. The photo  $V$ – $I$  curves were measured and recorded via a semiconductor parameter analyzer.

## AUTHOR INFORMATION

### Corresponding Author

\*E-mail: chho@mail.ntust.edu.tw. Tel: +886 2 27303772. Fax: +886 2 27303733.

## ACKNOWLEDGMENT

This work was sponsored by the National Science Council of Taiwan under the grant no. NSC98-2221-E-011-151-MY3.

## REFERENCES

- (1) Shen, G.; Liang, B.; Wang, X.; Huang, H.; Chen, D.; Wang, Z. L. Ultrathin  $\text{In}_2\text{O}_3$  Nanowires with Diameters below 4 nm: Synthesis, Reversible Wettability Switching Behavior, and Transparent Thin-Film Transistor Applications. *ACS Nano* **2011**, *5*, 6148–6155.
- (2) Lin, J.; Huang, Y.; Bando, Y.; Tang, C.; Li, C.; Golberg, D. Synthesis of  $\text{In}_2\text{O}_3$  Nanowire-Decorated  $\text{Ga}_2\text{O}_3$  Nanobelt Heterostructures and Their Electrical and Field-Emission Properties. *ACS Nano* **2010**, *4*, 2452–2458.
- (3) Shen, G.; Chen, D. Fast-Heating-Vapor-Trapping Method to Aligned Indium Oxide Bi-crystalline Nanobelts Arrays and Their Electronic Properties. *J. Mater. Chem.* **2010**, *20*, 10888–10893.
- (4) Lim, T.; Lee, S.; Meyyappan, M.; Ju., S. Control of Semiconducting and Metallic Indium Oxide Nanowires. *ACS Nano* **2011**, *5*, 3917–3922.
- (5) Shen, G.; Liang, B.; Wang, X.; Chen, P. C.; Zhou, C. Indium Oxide Nanospirals Made of Kinked Nanowires. *ACS Nano* **2011**, *5*, 2155–2161.
- (6) Dixit, A.; Sudakar, C.; Naik, R.; Naik, V. M.; Lawes, G. Undoped Vacuum Annealed  $\text{In}_2\text{O}_3$  Thin Films as a Transparent Conducting Oxide. *Appl. Phys. Lett.* **2009**, *95*, 195105.
- (7) Bahoura, M.; Lee, A.; Mundle, R.; Konda, R. B.; Kogo, G.; Bamiduro, O.; Yasar, O.; Moore, W.; Zhang, K.; Williams, F.; Pradhan, A. K. Ultraviolet Radiation Sensing in Composite Oxide Semiconductor Films. *Appl. Phys. Lett.* **2008**, *93*, 222112.
- (8) Cao, H.; Qiu, X.; Liang, Y.; Zhu, Q. Room-Temperature Ultraviolet-Emitting  $\text{In}_2\text{O}_3$  Nanowires. *Appl. Phys. Lett.* **2003**, *83*, 761–763.
- (9) Hartnagel, H. L.; Dawar, A. L.; Jain, A. K.; Jagadish, C. *Semiconducting Transparent Thin Films*; Institute of Physics: Bristol, U. K., 1995.
- (10) Huang, C. Y.; Lin, G. C.; Wu, Y. J.; Lin, T. Y.; Yang, Y. J.; Chen, Y. F. Efficient Light Harvesting by Well-Aligned  $\text{In}_2\text{O}_3$  Nanopushpins as Antireflection Layer on Si Solar Cells. *J. Phys. Chem. C* **2011**, *115*, 13083–13087.
- (11) Wang, G.; Park, J.; Wexler, D.; Park, M. S.; Ahn, J.-H. Synthesis, Characterization, and Optical Properties of  $\text{In}_2\text{O}_3$  Semiconductor Nanowires. *Inorg. Chem.* **2007**, *46*, 4778–4780.
- (12) Hsin, C. L.; He, J. H.; Lee, C. Y.; Wu, W. W.; Yeh, P. H.; Chen, L. J.; Wang, Z. L. Lateral Self-Aligned p-Type  $\text{In}_2\text{O}_3$  Nanowire Arrays Epitaxially Grown on Si Substrates. *Nano Lett.* **2007**, *7*, 1799–1803.
- (13) Liu, Q.; Lu, W.; Ma, A.; Tang, J.; Lin, J.; Fang, J. Study of Quasi-Monodisperse  $\text{In}_2\text{O}_3$  Nanocrystals: Synthesis and Optical Determination. *J. Am. Chem. Soc.* **2005**, *127*, 5276–5277.
- (14) Epifani, M.; Siciliano, P.; Gurlo, A.; Barsan, N.; Weimar, U. Ambient Pressure Synthesis of Corundum-Type  $\text{In}_2\text{O}_3$ . *J. Am. Chem. Soc.* **2005**, *126*, 4078–4079.
- (15) Lee, C. H.; Kim, M.; Kim, T.; Kim, A.; Paek, J.; Lee, J. W.; Choi, S. Y.; Kim, K.; Park, J. B.; Lee, K. Ambient Pressure Synthesis of Size-Controlled Corundum-Type  $\text{In}_2\text{O}_3$  Nanocubes. *J. Am. Chem. Soc.* **2006**, *128*, 9326–9327.
- (16) Dong, H.; Chen, Z.; Liaoxin, S.; Liang, Z.; Ling, Y.; Yu, C.; Tan, H. H.; Jagadish, C.; Shen, X. Nanosheets-Based Rhombohedral  $\text{In}_2\text{O}_3$  3D Hierarchical Microspheres: Synthesis, Growth Mechanism, and Optical Properties. *J. Phys. Chem. C* **2009**, *113*, 10511–10516.
- (17) Farvid, S. S.; Dave, N.; Radovanovic, P. V. Phase-Controlled Synthesis of Colloidal  $\text{In}_2\text{O}_3$  Nanocrystals via Size-Structure Correlation. *Chem. Mater.* **2010**, *22*, 9–11.
- (18) King, P. D. C.; Veal, F. F.; Wang, Ch. Y.; Payne, D. J.; Bourlange, A.; Zhang, H.; Bell, G. R.; Cimalla, V.; Ambacher, O.; Egdel, R. G.; Bechstedt, F.; McConville, C. F. Band Gap, Electronic Structure, and Surface Electron Accumulation of Cubic and Rhombohedral  $\text{In}_2\text{O}_3$ . *Phys. Rev. B* **2009**, *79*, 205211.
- (19) Walsh, A.; Da Silva; Juarez, L. F.; Wei, S. H.; Körber, C.; Klein, A.; Piper, L. F. J.; DeMasi, A.; Smith, K. E.; Panaccione, G.; Torelli, P.; Payne, D. J.; Bourlange, A.; Egdel, R. G. Nature of the band Gap of  $\text{In}_2\text{O}_3$  Revealed by First-Principles Calculations and X-Ray Spectroscopy. *Phys. Rev. Lett.* **2008**, *100*, 167402.
- (20) Bourlange, A.; Payne, D. J.; Egdel, R. G.; Foord, J. S.; Edward, P. P.; Jones, M. O.; Schertel, A.; Dobson, P. J.; Hutchison, J. L. Growth of  $\text{In}_2\text{O}_3$  (100) on Y-stabilized  $\text{ZrO}_2$  (100) by O-plasma Assisted Molecular Beam Epitaxy. *Appl. Phys. Lett.* **2008**, *92*, 092117.
- (21) Moss, T. S. The Interpretation of The Properties of Indium Antimonide. *Proc. Phys. Soc., London, Sect. B* **1954**, *67*, 775.
- (22) Bierwagen, O.; Speck, J. S.; Nagata, T.; Chikyow, T.; Yamashita, Y.; Yoshikawa, Y.; Yoshikawa, H.; Kobayashi, K. Depletion of The  $\text{In}_2\text{O}_3$  (001) and (111) Surface Electron Accumulation by an Oxygen Plasma Surface Treatment. *Appl. Phys. Lett.* **2011**, *98*, 172101.
- (23) Walsh, A.; Catlow, C. R. A.; Zhang, K. H. L.; Egdel, R. G. Control of The Band-Gap States of Metal Oxides by The Application of Epitaxial Strain: The Case of Indium Oxide. *Phys. Rev. B* **2011**, *83*, 161202(R).
- (24) Weither, R. L.; Ley, R. P. Optical Properties of Indium Oxide. *J. Appl. Phys.* **1966**, *37*, 299–302.
- (25) Liu, B.; Chen, R.; Xu, X. L.; Li, D. H.; Zhao, Y. Y.; Shen, Z. X.; Xiong, Q. H.; Sun, H. D. Exciton-Related Photoluminescence and Lasing in  $\text{CdS}$  Nanobelts. *J. Phys. Chem. C* **2011**, *115*, 12826–12830.
- (26) Nonoguchi, Y.; Nakashima, T.; Kawai, T. Temperature-Dependent Recombination Dynamics of  $\text{CdTe}$  Nanocrystals. *J. Phys. Chem. C* **2008**, *112*, 19263–19267.
- (27) Ketter, B.; Heiss, M.; Uccelli, E.; Arbiol, J.; Morral, A. F. Untangling the Electronic Band Structure of Wurtzite GaAs Nanowires by Resonant Raman Spectroscopy. *ACS Nano* **2011**, *5*, 7585–7592.
- (28) Matatagui, E.; Thompson, A. G.; Cardona, M. Thermoreflectance in Semiconductors. *Phys. Rev.* **1968**, *176*, 950–960.
- (29) Ho, C. H. Thermoreflectance Characterization of Band-Edge Excitonic Transitions in  $\text{CuAlS}_2$  Ultraviolet Solar-Cell Material. *Appl. Phys. Lett.* **2010**, *96*, 061902.
- (30) Ho, C. H. Enhanced Photoelectric-Conversion Yield in Niobium-incorporated  $\text{In}_2\text{S}_3$  with Intermediate Band. *J. Mater. Chem.* **2011**, *21*, 10518–10524.
- (31) Aspnes, D. E. in *Handbook on Semiconductors*; Balkanski, M., Ed.; North Holland: Amsterdam, 1980.
- (32) Yan, Y. G.; Zhang, Y.; Zeng, H. B.; Zhang, L. D.  $\text{In}_2\text{O}_3$  Nanotowers: Controlled Synthesis and Mechanism Analysis. *Cryst. Growth Des.* **2007**, *7*, 940–943.
- (33) Yin, W.; Cao, M.; Luo, S.; Hu, C.; Wei, B. Controllable Synthesis of Various  $\text{In}_2\text{O}_3$  Submicron/Nanostructures Using Chemical Vapor Deposition. *Cryst. Growth Des.* **2009**, *9*, 2173–2178.
- (34) Maestre, D.; Häussler, D.; Cremades, A.; Jäger, W.; Piqueras, J. Nanopipes in  $\text{In}_2\text{O}_3$  Nanorods Grown by Thermal Treatment. *Cryst. Growth Des.* **2011**, *11*, 1117–1121.
- (35) Jean, S. T.; Her, Y. C. Growth Mechanism and Photoluminescence Properties of  $\text{In}_2\text{O}_3$  Nanotowers. *Cryst. Growth Des.* **2010**, *10*, 2104–2110.
- (36) Hao, Y.; Meng, G.; Ye, C.; Zhang, L. Controlled Synthesis of  $\text{In}_2\text{O}_3$  Octahedrons and Nanowires. *Cryst. Growth Des.* **2005**, *5*, 1617–1621.
- (37) Chen, C. J.; Xu, W. L.; Chern, M. Y. Low-Temperature Epitaxial Growth of Vertical  $\text{In}_2\text{O}_3$  Nanowires on A-Plane Sapphire with Hexagonal Cross-Section. *Adv. Mater.* **2007**, *19*, 3012–3015.
- (38) Ho, C. H.; Tsai, M. C.; Wong, M. S. Characterization of Indirect and Direct Interband Transitions of Anatase  $\text{TiO}_2$  by Thermoreflectance Spectroscopy. *Appl. Phys. Lett.* **2008**, *93*, 081904.
- (39) Pollak, F. H.; Shen, H. Modulation Spectroscopy of Semiconductors: Bulk/Thin Film, Microstructures, Surfaces/Interfaces and Devices. *Mater. Sci. Eng., R* **1993**, *10*, 275–374.



- (40) Long, R.; English, N. J. Electronic Structure and Origin of Visible-Light Activity of C-Doped Cubic  $\text{In}_2\text{O}_3$  From First-Principles Calculations. *J. Phys. Chem. C* **2010**, *114*, 13942–13946.
- (41) Wei, Z. P.; Guo, D. L.; Liu, B.; Chen, R.; Wong, L. M.; Yang, W. F.; Wang, S. J. Ultraviolet Light Emission and Excitonic Fine Structures in Ultrathin Single-Crystalline Indium Oxide Nanowires. *Appl. Phys. Lett.* **2010**, *96*, 031902.
- (42) Yu, P. Y.; Cardona, M. In *Fundamentals of Semiconductors, Physics and Materials Properties*, 3rd ed.; Springer-Verlag: Berlin, 2001.
- (43) King, P. D. C.; Veal, T. D.; Payne, D. J.; Bourlange, A.; Egdel, R. G.; McConville, C. F. Surface Electron Accumulation and the Charge Neutrality Level in  $\text{In}_2\text{O}_3$ . *Phys. Rev. Lett.* **2008**, *101*, 116808.
- (44) Ho, C. H.; Tseng, C. Y.; Tien, L. C. Thermoreflectance Characterization of  $\beta\text{-Ga}_2\text{O}_3$  Thin-Film Nanostrips. *Opt. Express* **2010**, *18*, 16360–16369.
- (45) Wu, X. C.; Hong, J. M.; Han, Z. J.; Tao, Y. R. Fabrication and Photoluminescence Characteristics of Single Crystalline  $\text{In}_2\text{O}_3$  Nanowires. *Chem. Phys. Lett.* **2003**, *373*, 28–32.
- (46) Tahar, R. B. H.; Ban, T.; Ohya, Y.; Takahashi, Y. Optical, Structural, and Electrical Properties of Indium Oxide Thin Films Prepared by the Sol-Gel Method. *J. Appl. Phys.* **1997**, *82*, 865–870.
- (47) Peng, X. S.; Meng, G. W.; Zhang, J.; Wang, X. F.; Wang, Y. W.; Wang, C. Z.; Zhang, L. D. Synthesis and Photoluminescence of Single Crystalline  $\text{In}_2\text{O}_3$  Nanowires. *J. Mater. Chem.* **2002**, *12*, 1602–1605.
- (48) Fuchs, F.; Bechstedt, F. Indium-Oxide Polymorphs from First Principles: Quasiparticle Electronic States. *Phys. Rev. B* **2008**, *77*, 155107.
- (49) Gao, J.; Chen, R.; Li, D. H.; Jiang, L.; Ye, J. C.; Ma, X. C.; Chen, X. D.; Xiong, Q. H.; Sun, H. D.; Wu, T. UV Light Emitting Transparent Conducting Tin-doped Indium Oxide (ITO) Nanowires. *Nanotechnology* **2011**, *22*, 195706.
- (50) Masuda, Y.; Kondo, M.; Koumoto, K. Site-Selective Deposition of  $\text{In}_2\text{O}_3$  Using a Self-Assembled Monolayer. *Cryst. Growth Des.* **2009**, *9*, 555–561.
- (51) Wagner, R. S.; Ellis, W. C. Vapor-Liquid-Solid Mechanism of Single Crystal Growth. *Appl. Phys. Lett.* **1964**, *4*, 89–90.
- (52) Ho, C. H.; Lee, H. W.; Cheng, Z. H. Practical Thermoreflectance Design for Optical Characterization of Layer Semiconductors. *Rev. Sci. Instrum.* **2004**, *75*, 1098–1102.
- (53) Ho, C. H.; Chen, Y. J.; Jhou, H. W.; Du, J. H. Optical Anisotropy of  $\text{ZnO}$  Nanocrystals on Sapphire by Thermoreflectance Spectroscopy. *Opt. Lett.* **2007**, *32*, 2765–2767.